Efficient circularly polarized electroluminescence from achiral luminescent materials

Letian Xu,[1] Hao Liu,[1] Xiaoluo Peng,[1] Pingchuan Shen,[1] Ben Zhong Tang[2] and Zujin Zhao*,[1]

[1] State Key Laboratory of Luminescent Materials and Devices, Guangdong Provincial Key Laboratory of Luminescence from Molecular Aggregates, South China University of Technology, 510640 Guangzhou, China. E-mail: mszjzhao@scut.edu.cn

[2] School of Science and Engineering, Shenzhen Institute of Aggregate Science and Technology, The Chinese University of Hong Kong, Shenzhen, Guangdong 518172, China.

Abstract

Circularly polarized electroluminescence (CP-EL) with a defined color is generally produced in organic light-emitting diodes (OLEDs) based on CP luminescent (CPL) materials with similar colors. Such kind of many-to-many relationship requires numerous new CPL materials to fabricate CP-OLEDs because the well-developed achiral luminescent materials are rarely considered to be capable of directly producing CP-EL. Herein, the one-to-many strategy is proposed for CP-EL by employing high-performance near ultraviolet CPL materials to sensitize achiral luminescent materials. These newly developed near ultraviolet CPL materials have excellent photoluminescence (PL) quantum yields and good CPL dissymmetry factors, and can induce efficient blue to red CP-PL for achiral fluorescence, phosphorescence, thermally activated delayed fluorescence (TADF) and multi-resonance (MR) TADF materials. Efficient near ultraviolet CP-EL with the best external quantum efficiencies (η_{ext}s) of 9.0% at 404 nm and extremely small efficiency roll-offs are achieved by using them as emitters for CP-OLEDs. By adopting them as hosts or sensitizers, commercially available yellow-orange achiral phosphorescence, TADF and MR-TADF materials can generate strong CP-EL, with absolute dissymmetry factors and outstanding η_{ext}s of up to 2.87×10^{-3} and 30.8%, respectively, which are the state-of-the-art CP-EL performances reported so far, demonstrating a simple and universal avenue towards efficient CP-EL.

Introduction

Circularly polarized electroluminescence (CP-EL) has drawn extensive attention owing to its direct asymmetrical emission of left- or right-hand circularly polarized light, which has diverse applications in frontier high-tech fields such as 3D display, quantum computing, and so forth[1-5]. To realize CP-EL, developing efficient light-emitting materials with circularly polarized luminescence (CPL) for the fabrication of organic light-emitting diodes (OLEDs) is of high importance[6-11]. Generally, CP-EL with a defined color is acquired from corresponding CPL materials with similar colors, which means a great number of CPL materials are required in OLEDs to fulfill the need of CP-EL in varied color regions[12-16]. Currently, great efforts have been devoted to explore numerous new CPL materials to meet such kind of many-to-many relationship[17-22]. These CPL materials are basically built by introducing chiral groups to molecular frameworks responsible for light emission *via* chiral perturbation, or constructing a chiral center directly in a rigid luminescent framework[23-29]. These approaches often involve complicated synthetic procedures, but the CP-EL efficiencies of the resultant materials are not always satisfactory. Actually, a library of high-performance achiral EL materials, such as phosphorescence and thermally activated delayed fluorescence (TADF) materials, have been well-developed, and many of them have been commercialized, but they are rarely considered to be capable of direct producing CP-EL in previous researches.

In photoluminescence (PL) process, achiral chromophores were reported to acquire CP-PL signals from CPL

materials, presumably *via* Förster resonance energy transfer (FRET) mechanism[30-33]. This phenomenon is envisioned to be applicable in OLEDs to achieve CP-EL for achiral luminescent materials, based on which a one-to-many strategy can be imaged. In that case, a great number of well-developed EL materials can be adopted to fabricate CP-OLEDs, providing a simple and universal approach towards CP-EL with varied colors. The difficulty of this strategy lies in exploring efficient CPL materials with high PL quantum yields (Φ_{PL}s), high exciton utilization and sufficiently short emission wavelengths (ideally < 450 nm) to function as CPL sources[34]. Recently, purely organic CPL materials with TADF feature are reported as good candidates for realizing efficient CP-EL because of their full exciton utilization based on reverse intersystem crossing (RISC) process[35-37]. But due to strong intramolecular charge transfer (ICT) effect, the reported CP-TADF materials only show emission peaks in the range of 453–716 nm[38-41], and those with emission peaks shorter than 450 nm are rarely achieved.

In this work, the one-to-many strategy for attaining CP-EL is proposed by employing a series of new efficient near ultraviolet CPL materials to sensitize various achiral luminescent materials (Fig. 1). These near ultraviolet CPL materials are designed by introducing chiral groups of *S*/*R*-1,1'-bi-2-naphthol (*S*/*R*-BN) to a conjugated molecular skeleton consisting of benzonitrile acceptor, carbazole donor and phenyl bridge. The *S*/*R*-BN groups are linked to benzonitrile acceptor to not only endow the molecule with CPL property but also weaken ICT effect for short-wavelength emission. The resultant materials exhibit distinguished advantages of prominent CPL signals, excellent Φ_{PL}s and high exciton utilization based on high-level RISC (hRISC) mechanism, which enable them to perform efficiently in CP-OLEDs, rendering near ultraviolet CP-EL and maximum external quantum efficiencies ($\eta_{ext,max}$s) of up to 9.0% at 404 nm with very small efficiency roll-offs. To the best of our knowledge, these are the best CPL materials with emission peaks at <430 nm reported so far. More importantly, they can sensitize commercially available achiral luminescent materials, such as phosphorescence, TADF and MR-TADF materials, to achieve highly efficient CP-OLEDs with outstanding $\eta_{ext,max}$s and good dissymmetry factors, demonstrating a simple and universal strategy for efficient CP-EL has been successfully established.

Results

The target materials can be facilely prepared according to the synthetic routes illustrated in Supplementary Scheme 1, and their structures are verified by NMR, high-resolution mass spectrometry and X-ray single-crystal diffraction. According to crystal structures, these materials favor twisted conformations with perfect mirror symmetry as exemplified by *S*/*R*-BNPCN-*o*-TBCP (Supplementary Fig. 1). Close molecular packing is prevented in these materials, which is conducive to suppressing strong intermolecular interaction and alleviating emission quenching and exciton annihilation in film state. They have high decomposition temperatures of 437–446 °C, indicative of good thermal stability. A high glass-transition temperature of 225 °C observed for *S*-BNPCN-*p*-TBCP suggests its good morphological stability (Supplementary Fig. 2). They also exhibit good electrochemical stability, as evidenced by reversible oxidation and reduction processes in cyclic voltammetry experiment (Supplementary Fig. 3). The energy levels of the highest occupied molecular orbital (HOMO) and the lowest unoccupied molecular orbital (LUMO) are calculated as –5.46~–5.66 and –2.48~–2.58 eV, respectively, from onset potentials of oxidation and reduction waves.

In view of the almost identical properties of the *S*/*R*-enantiomers, the molecules with *S*-configuration are taken as examples for photophysical property investigation. According to geometrical and electronic structures simulated by theoretical calculation[42], the HOMOs and LUMOs are basically distributed on carbazole and benzonitrile, respectively, but they show apparent overlaps on the phenyl bridge (Fig. 1c and Supplementary Fig. 4a). The insufficient separation of HOMOs and LUMOs causes large theoretical energy gaps of 0.84–0.92 eV between the lowest excited triplet (T_1) and singlet (S_1) states, indicating typical RISC process from T_1 to S_1 states can hardly occur in these materials. Nevertheless, the energy gaps between high-lying excited triplet (T_4–T_6) states and S_1 state are really small (0.09–0.19 eV), while the energy gaps between T_3 and T_4 states are quite large (0.42–0.49 eV).

Meanwhile, there are considerable spin-orbital coupling (SOC) matrix elements between T_4–T_6 and S_1 states (Fig. 1c and Supplementary Fig. 4b). Taking these factors into consideration, hRISC process is very likely to happen. The theoretical simulation of *S*-BNPCN-*o*-CP in solid state by QM/MM[43] method is further performed. As shown in Fig. 1c, the energy levels are similar to those in gas phase, with the energy gaps between T_4–T_6 and S_1 states as small as 0.01–0.07 eV, while that between T_1 and S_1 states is increased to 0.83 eV. Moreover, the SOC matrix elements between S_1 and T_5–T_6 states are enhanced in solid state. The calculated radiative decay rate of *S*-BNPCN-*o*-CP in

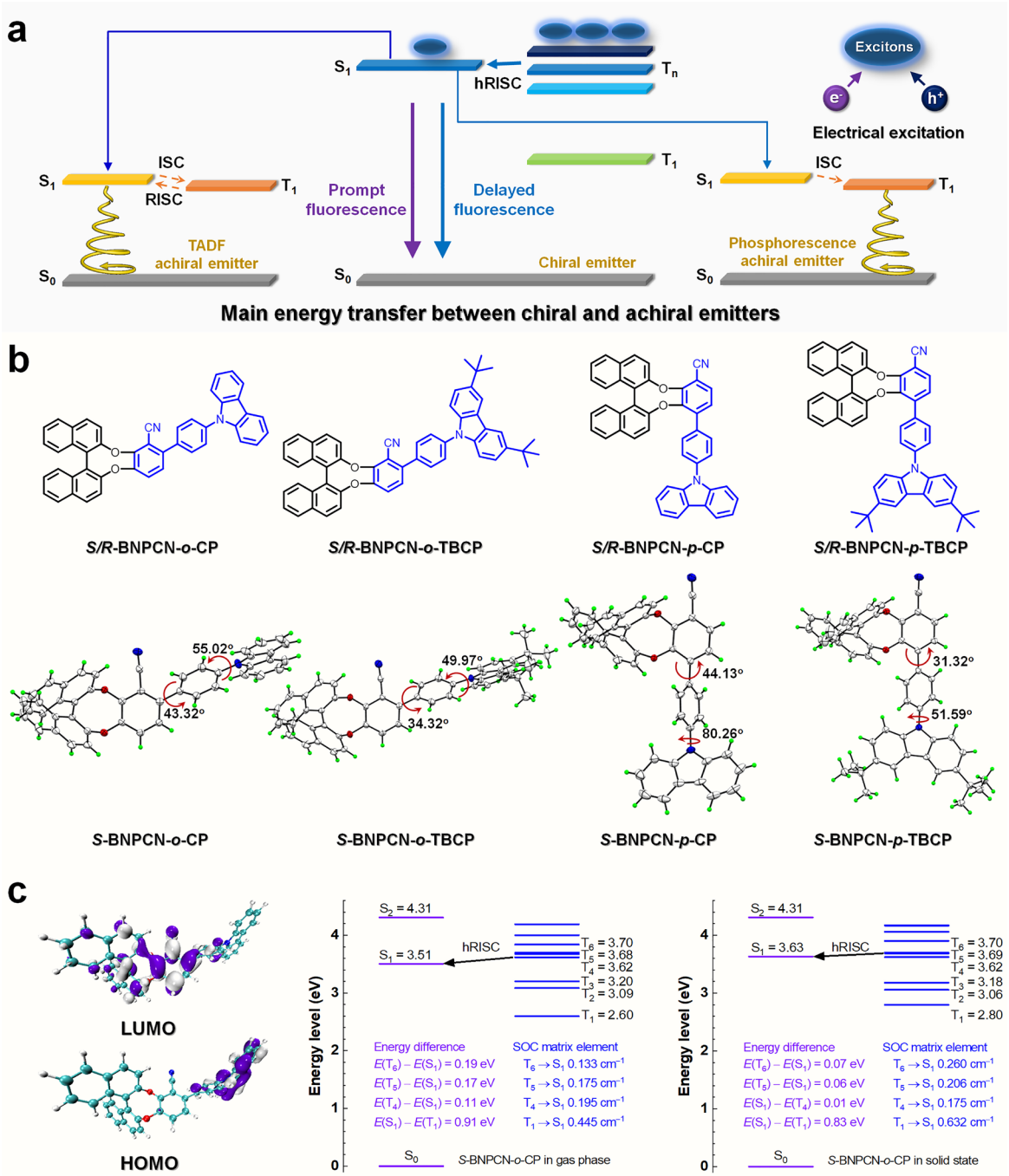

Fig. 1 | Design concept of efficient CP-EL based on chiral and achiral luminescent molecules. **a**, The main energy transfer processes between chiral and achiral materials. **b**, Molecular and crystal structures of the new near ultraviolet CPL materials. **c**, HOMO and LUMO distribution of *S*-BNPCN-*o*-CP, and energy levels and SOC matrix elements of *S*-BNPCN-*o*-CP in gas phase and in solid state.

solid state (3.87×10^8 S^{-1}) is close to that in gas phase (5.31×10^8 S^{-1}), but the non-radiative decay rate in solid state (2.62×10^7 S^{-1}) is much smaller than that in gas phase (2.06×10^8 S^{-1}). These results indicate that hRISC process can be promoted in solid state[44].

S-BNPCN-*o*-CP and *S*-BNPCN-*p*-CP exhibit similar absorption maxima at ~330 nm with absorption tails ending at ~380 nm (Fig. 2a), and show close PL peaks at ~400 nm in dilute toluene solutions (Fig. 2b). *S*-BNPCN-*o*-TBCP and *S*-BNPCN-*p*-TBCP have red-shifted absorption maxima (~350 nm) and PL peaks (411 and 415 nm) (Table 1), due to the enhanced ICT effect caused by the additional electron-pushing *tert*-butyl groups on carbazole donors. In neat films, *S*-BNPCN-*o*-CP, *S*-BNPCN-*p*-CP, *S*-BNPCN-*o*-TBCP and *S*-BNPCN-*p*-TBCP show strong PL emissions peaking at 418, 420, 429 and 431 nm, with excellent Φ_{PL}s of 90%, 93%, 85% and 88%, respectively, higher than

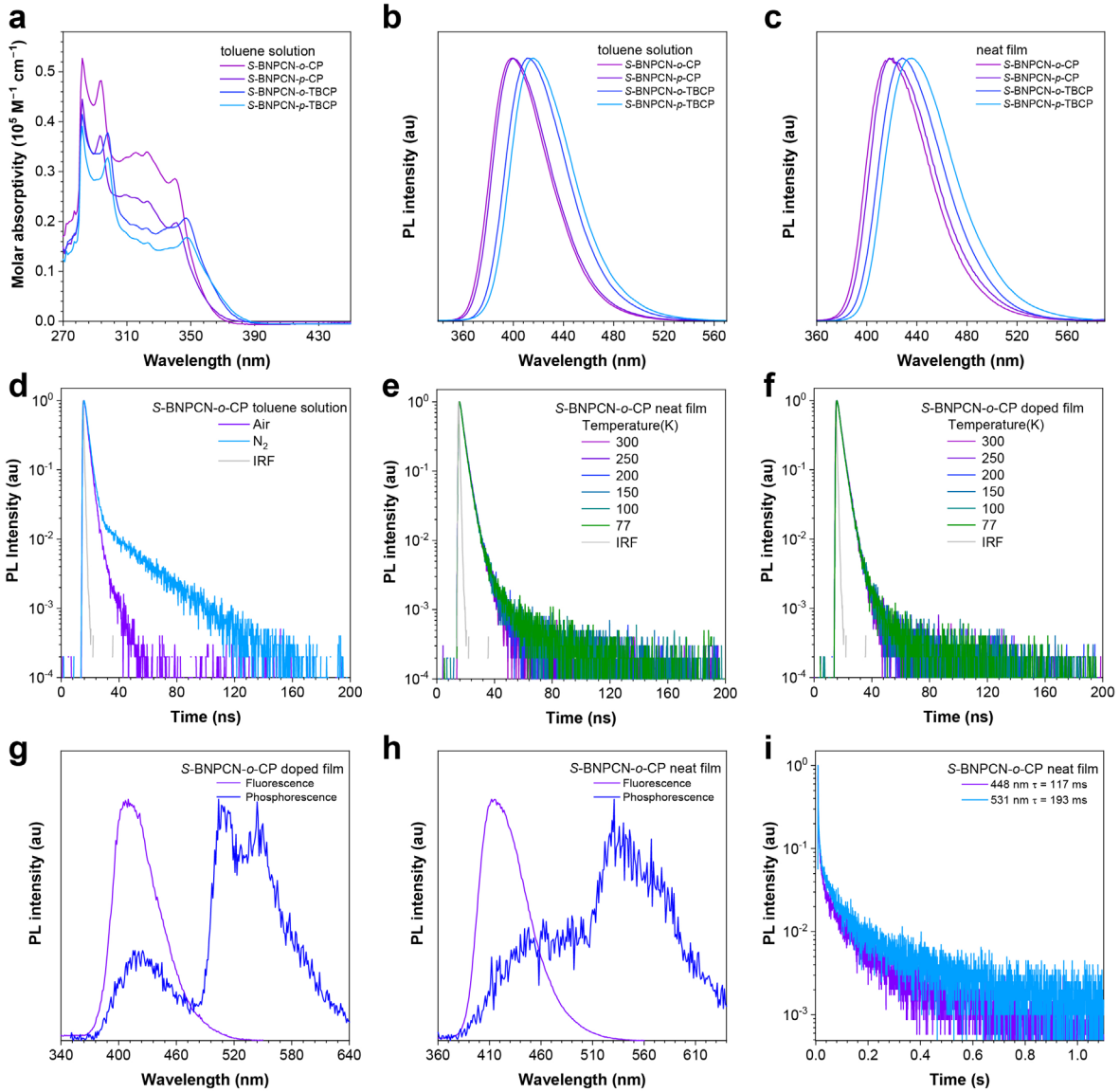

Fig. 2 | Photophysical properties of the near ultraviolet CPL materials. a, UV-vis absorption spectra and PL spectra of *S*-BNPCN-*o*-CP, *S*-BNPCN-*p*-CP, *S*-BNPCN-*o*-TBCP and *S*-BNPCN-*p*-CP **b**, in toluene (1×10^{-5} M) and **c**, neat films. **d**, Transient PL decay spectrum of *S*-BNPCN-*o*-CP in toluene (1×10^{-5} M). Temperature-dependent transient PL decay spectra of **e**, neat film and **f**, doped film of *S*-BNPCN-*o*-CP, measured under nitrogen (IRF = instrument response function). The excitation wavelength is 280 nm. Fluorescence and phosphorescence spectra of **g**, doped film and **h**, neat film of *S*-BNPCN-*o*-CP measured at 77 K. **i**, Transient PL decay spectrum of neat film of *S*-BNPCN-*o*-CP measured at 77 K. The excitation wavelength was 320 nm.

those in toluene solutions (77%–81%) (Fig. 2c, Table 1). By doping these materials into 2,8-bis(diphenylphosphoryl)dibenzo(b,d)furan (PPF) host with a concentration of 50 wt%, their PL spectra are almost identical and the Φ_{PL}s are slightly changed relative to those in neat films (Table 1), indicating they are free of concentration- or aggregation-caused emission quenching.

The solvatochromic effect is studied in different solvents with varied polarity to explore the electronic structures, by taking *S*-BNPCN-*o*-CP and *S*-BNPCN-*p*-CP as examples. The PL peaks of *S*-BNPCN-*o*-CP and *S*-BNPCN-*p*-CP are red-shifted from 376 and 370 nm in low-polar hexane to 465 and 474 nm in high-polar acetonitrile (Supplementary Fig. 5), respectively, due to enhanced ICT effect. Linear relationships between Stokes shift ($\nu_a - \nu_f$) and solvent polarity (*f*) fitted by the Lippert–Mataga model (Supplementary Fig. 5, Supplementary Table 1 and 2) suggest that they have a quasi-equivalent hybridization character originating from a balanced intercrossed coupling between locally excited and charge transfer states, which is beneficial for achieving high emission efficiency and high exciton utilization simultaneously[45-47].

The transient PL decay spectra disclose the *S*-enantiomers in toluene solutions experience double exponential decay processes under nitrogen with short mean PL lifetimes of 5.5–7.2 ns. Apparent delayed components with long lifetimes of 24.3–28.4 ns are observed under nitrogen, but the delayed components become weak with lifetimes reduced to 6.2–6.8 ns under air (Fig. 2, Supplementary Fig. 6 and Supplementary Table 3), indicative of the participation of triplet excited states in radiative decay process. In neat films, they show short mean PL lifetimes of 3.0–4.1 ns with decreased but discernable delayed components. The lifetimes of delayed components are shortened to 5.2–7.6 ns under nitrogen, but get slightly prolonged by increasing temperature from 77 to 300 K, as revealed by the temperature-dependent transient PL decay spectra (Fig. 2 and Supplementary Fig. 7). Similar trend is also observed for these materials in doped films (Supplementary Table 4 and 5). Compared to the delayed lifetimes of up to microsecond level of typical TADF materials, the delayed lifetimes of these materials are apparently too short.

Table 1 | Photophysical properties of the near ultraviolet CPL materials

	solution[a]						neat film/doped film[b]					
	λ_{abs} (nm)	λ_{em} (nm)	Φ_F[c] (%)	τ[d] (ns)	τ_p[d] (ns)	τ_d[d] (ns)	λ_{em} (nm)	Φ_F[c] (%)	τ[d] (ns)	τ_p[d] (ns)	τ_d[d] (ns)	ΔE_{ST}[e] (eV)
S-BNPCN-*o*-CP	323	399	79	5.5	2.4	24.3	418/414	90/91	3.0/3.1	2.4/2.7	5.2/5.2	0.67/0.56
S-BNPCN-*p*-CP	323	400	81	6.3	2.6	27.2	420/421	93/93	3.4/3.8	2.7/3.3	6.7/8.4	0.61/0.55
S-BNPCN-*o*-TBCP	347	411	77	6.4	3.0	26.3	429/431	85/89	3.6/4.3	2.8/3.6	6.1/7.9	0.61/0.53
S-BNPCN-*p*-TBCP	348	415	80	7.2	3.2	28.4	431/433	88/92	4.1/4.4	3.1/3.5	7.6/9.8	0.52/0.46

[a] Measured in toluene solution at room temperature. [b] Vacuum-deposited on a quartz substrate; the doping concentration is 50 wt% in PPF. [c] Determined by a calibrated integrating sphere under nitrogen at room temperature. [d] τ = mean PL lifetime; τ_p = prompt lifetime; τ_d = delayed lifetime; evaluated at 300 K under nitrogen. [e] Estimated from the peaks of fluorescence and phosphorescence spectra at 77 K.

To further understand the working mechanism of photophysical property, the fluorescence and phosphorescence spectra of the neat films of *S*-enantiomers are collected at 77 K to calculate S_1–T_1 energy splitting (ΔE_{ST}) (Fig. 2 and Supplementary Fig. 8). Interestingly, each *S*-enantiomer shows one fluorescence peak but two phosphorescence peaks, and the short-wavelength phosphorescence peak is red-shifted by ~30 nm relative to the fluorescence peak. For example, the phosphorescence spectrum of *S*-BNPCN-*o*-CP in neat film has two peaks at 448 and 531 nm, with different lifetimes of 117 and 193 ms, respectively. In consideration of the extraordinarily short delayed lifetimes of these materials, this short-wavelength phosphorescence peak at 448 nm is deduced to be associated with high-lying triplet excited states, which undergo hRISC process to convert to S_1 state, while the long-wavelength peak comes from T_1 state. Thus, the ΔE_{ST}s, calculated from the fluorescence peak and long-wavelength phosphorescence peak, are 0.52–0.67 eV for *S*-enantiomers in neat films. Similar phenomena are observed for their doped films in PPF host and the ΔE_{ST}s are calculated as 0.46–0.56 eV (Fig. 2 and Supplementary Fig. 9). These findings disclose that the typical TADF is absent in these materials, and the short delayed components should be induced by hRISC process[48], which is in good agreement with the theoretical calculation results.

Concerning the presence of chiral *S*/*R*-BN groups, the chiroptical property of these materials in the ground state are investigated initially by employing Circular Dichroism (CD) spectra in dilute solutions. As shown in Fig. 3b and Supplementary Fig. 10, the *S*/*R*-enantiomers show mirror-image bands with strong Cotton effects, indicative of prominent chirality. They also exhibit clear CP-PL signals in toluene solutions, which confirm the chiroptical property in the excited state. For example, *S*/*R*-BNPCN-*o*-CP show mirror-image CP-PL spectra with PL dissymmetry factors (g_{PL}) of -6.07×10^{-4} and 4.80×10^{-4}, respectively. The neat films of these materials also exhibit noticeable CP-PL signals with increased absolute g_{PL} values. For example, *S*/*R*-BNPCN-*o*-CP neat films have g_{PL} values of -2.40×10^{-3} and 2.63×10^{-3}, respectively, better than those in doped films (-5.75×10^{-4} and 5.61×10^{-4}) and in toluene

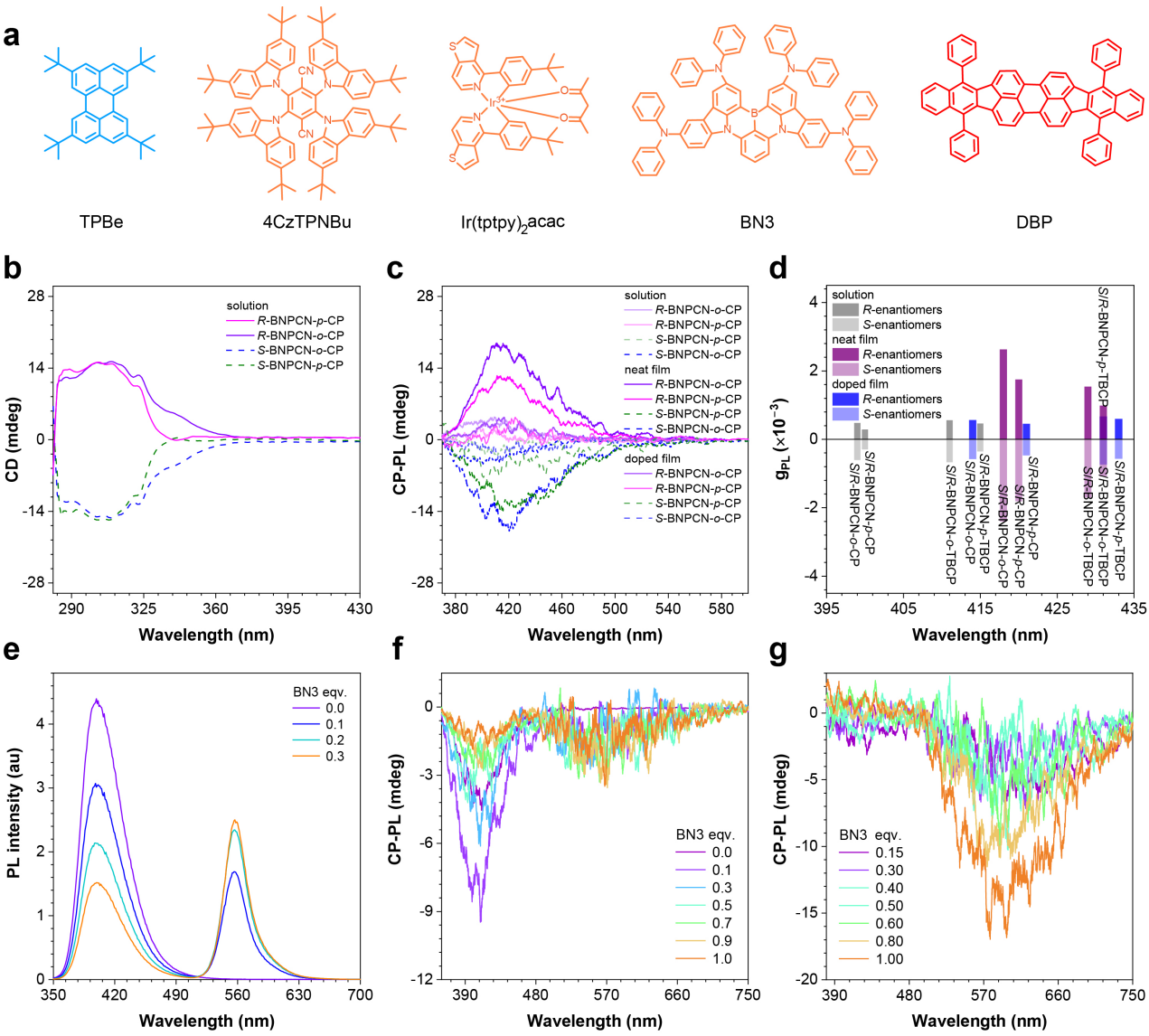

Fig. 3 | Chiral properties of the near ultraviolet CPL materials and FRET process. a, The molecular structures of achiral luminescent guest molecules. **b**, CD spectra of *S*/*R*-BNPCN-*o*-CP and *S*/*R*-BNPCN-*p*-CP in toluene (2.0×10^{-5} M). **c**, CP-PL spectra of *S*/*R*-BNPCN-*o*-CP and *S*/*R*-BNPCN-*p*-CP in toluene (1.0×10^{-5} M), neat films, and doped films (50 wt% in PPF). The excitation wavelength is 320 nm. **d**, g_{PL} values of the near ultraviolet CPL materials at their related PL peaks in toluene (1.0×10^{-5} M), neat films, and doped films (50 wt% in PPF). **e**, PL and **f**, CP-PL spectra of *S*-BNPCN-*o*-CP (3.0×10^{-5} M) loaded with different equivalents of BN3 in toluene. The excitation wavelength is 320 nm. **g**, CP-PL spectra of *S*-BNPCN-*o*-CP (20 wt% in PMMA) films loaded with different equivalents of BN3. The excitation wavelength is 340 nm.

solutions (Supplementary Table 6), probably due to more regular arrangement of the molecules in neat films.

Given the near-ultraviolet PL emissions of these materials, the energy transfer process from them to different kinds of long-wavelength achiral luminescent materials are subsequently studied[49-52], including fluorescence (TPBe and DBP), phosphorescence ($Ir(tptpy)_2acac$), TADF (4CzTPNBu) and MR-TADF (BN3) materials, whose absorption spectra are well overlapped with the PL spectrum of *S*-BNPCN-*o*-CP (Supplementary Fig. 11a). Delightfully, by exciting *S*-BNPCN-*o*-CP with 320 nm light, the toluene solutions containing *S*-BNPCN-*o*-CP (3.0×10^{-5} M) and achiral luminescent materials (6.0×10^{-6} M) show long-wavelength PL peaks from achiral luminescent materials, accompanied by detectable CP-PL signals (Supplementary Fig. 11b and Fig. 12). This finding implies FRET process occurs from *S*-BNPCN-*o*-CP to long-wavelength achiral luminescent materials, regardless of the luminescence nature[53-57]. To further study this phenomenon, the PL and CP-PL spectra are recorded for the mixed systems of BN3

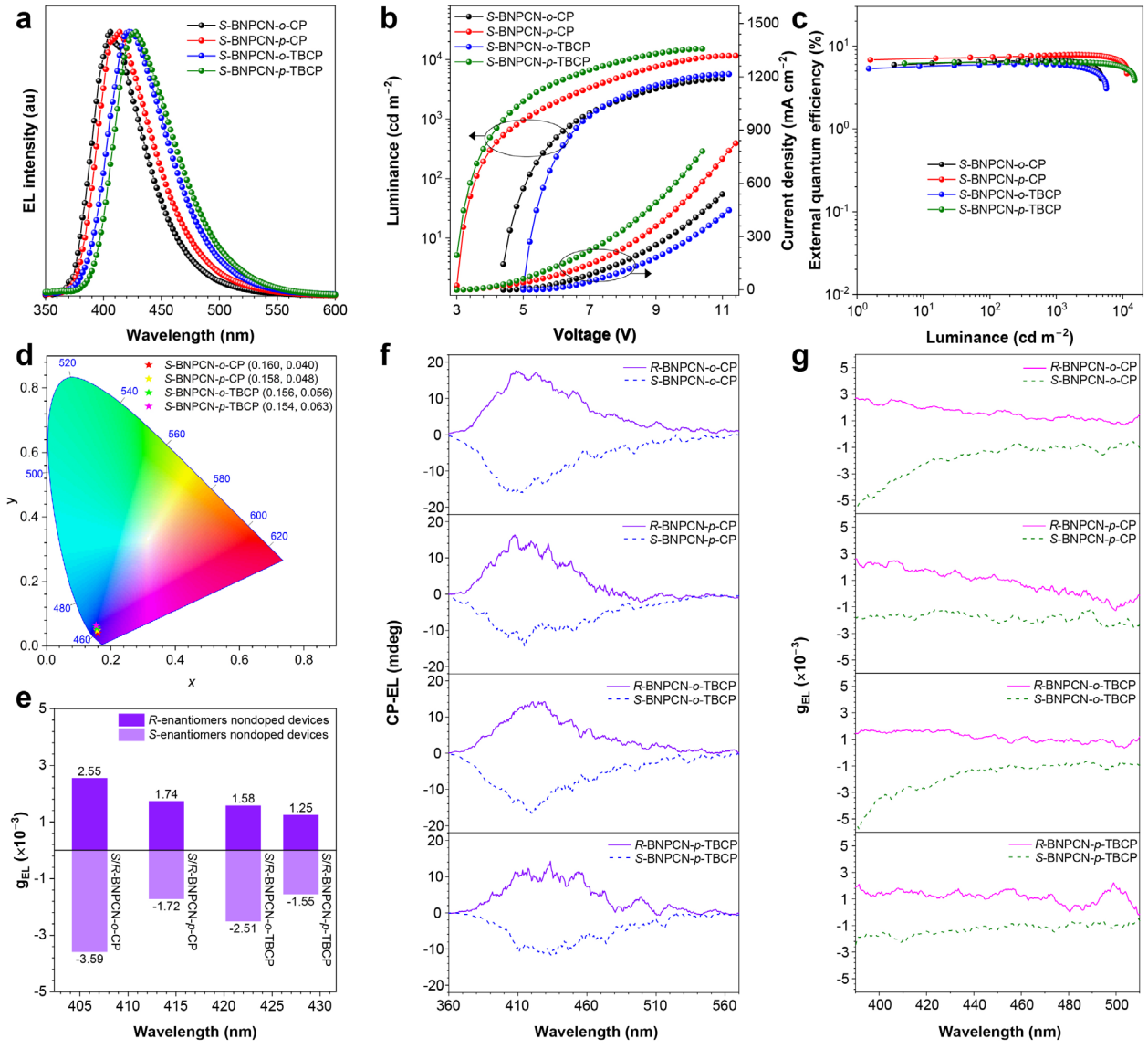

Fig. 4 | CP-EL performances of nondoped CP-OLEDs using the near ultraviolet CPL materials as emitters. a, EL spectra of *S*-BNPCN-*o*-CP, *S*-BNPCN-*p*-CP, *S*-BNPCN-*o*-TBCP and *S*-BNPCN-*p*-TBCP at 5 V. **b**, Plots of luminance–voltage–current density and **c**, external quantum efficiency–luminance of *S*-BNPCN-*o*-CP, *S*-BNPCN-*p*-CP, *S*-BNPCN-*o*-TBCP and *S*-BNPCN-*p*-TBCP in nondoped OLEDs. **d**, CIE color coordinates of nondoped OLEDs. **e**, g_{EL} of the nondoped OLEDs. **f**, CP-EL spectra collected under 4 V and **g**, plots of g_{EL} versus EL wavelength of nondoped OLEDs of *S*-BNPCN-*o*-CP, *S*-BNPCN-*p*-CP, *S*-BNPCN-*o*-TBCP and *S*-BNPCN-*p*-TBCP.

and *S*-BNPCN-*o*-CP in toluene solutions, under the excitation of 320 nm light. The PL peak of *S*-BNPCN-*o*-CP becomes weakened gradually by increasing BN3 concentration (Fig. 3e), indicative of FRET process from *S*-BNPCN-*o*-CP to BN3[58-60]. In the absence of BN3, only the CP-PL signal at ~400 nm from *S*-BNPCN-*o*-CP is observed, without other CP-PL signals. By increasing BN3 concentration, a new CP-PL signal appears and gets intensified at 556 nm (Fig. 3f), which stems from BN3. Afterward, this phenomenon is studied in film state. The achiral luminescent materials exhibit clear CP-PL signals at their corresponding PL wavelengths by doping them (3 wt%) no matter in *S*-BNPCN-*o*-CP and *S*-BNPCN-*p*-CP neat films or in poly(methyl methacrylate) (PMMA) film containing 5 wt% or 20 wt% *S*-BNPCN-*o*-CP (Fig. 3g, Supplementary Figs. 13-15). By increasing BN3 concentration in PMMA film doped with both BN3 and *S*-BNPCN-*o*-CP, the CP-PL signal from BN3 is enhanced accordingly, more obvious than that observed in toluene solutions (Supplementary Fig. 16). These results disclose that the CP-PL signals of the long-wavelength achiral luminescent materials is indeed induced by the short-wavelength CPL material during FRET process. Such kind of energy transfer process accompanied by the inducement of CP-PL signal may provide a facile and universal approach to realize CP-EL for achiral luminescent materials.

Table 2 | CP-EL performances of CP-OLEDs using *S*-enantiomers as emitters.[a)]

EML	V_{on} (V)	L_{max} (cd m^{-2})	η_{ext} (%)		λ_{EL} (nm)	CIE (x, y)	FWHM (nm)	g_{EL} (10^{-3})
			maximum	at 1000 cd m^{-2}				
S-BNPCN-o-CP	4.3	4743	6.7	6.6	406	(0.160, 0.040)	51	–3.59
S-BNPCN-*p*-CP	3.0	11570	7.8	7.8	414	(0.158, 0.048)	52	–1.72
S-BNPCN-*o*-TBCP	5.0	5663	6.1	5.9	422	(0.156, 0.056)	59	–2.51
S-BNPCN-*p*-TBCP	3.0	15110	6.4	6.4	428	(0.154, 0.063)	61	–1.55
50 wt% *S*-BNPCN-*o*-CP: PPF	3.2	4362	8.1	7.8	404	(0.162, 0.049)	54	–1.44
60 wt% *S*-BNPCN-*o*-CP: PPF	3.2	6843	9.0	8.5	404	(0.166, 0.066)	54	-
70 wt% *S*-BNPCN-*o*-CP: PPF	3.6	4367	8.5	8.3	406	(0.158, 0.036)	54	-
80 wt% *S*-BNPCN-*o*-CP: PPF	3.6	4670	8.3	8.2	406	(0.158, 0.037)	54	-
50 wt% *S*-BNPCN-*p*-CP: PPF	3.2	3866	6.8	6.2	406	(0.157, 0.040)	56	–1.70
60 wt% *S*-BNPCN-*p*-CP: PPF	3.2	4879	6.9	6.7	406	(0.157, 0.040)	56	-
70 wt% *S*-BNPCN-*p*-CP: PPF	3.0	9018	7.0	6.0	414	(0.157, 0.047)	57	-
80 wt% *S*-BNPCN-*p*-CP: PPF	3.0	9114	7.2	7.2	414	(0.157, 0.044)	57	-
50 wt% *S*-BNPCN-*o*-TBCP: PPF	3.4	6803	9.1	8.1	420	(0.155, 0.052)	62	–1.56
60 wt% *S*-BNPCN-*o*-TBCP: PPF	3.4	7193	8.9	8.3	422	(0.155, 0.052)	62	-
70 wt% *S*-BNPCN-*o*-TBCP: PPF	3.6	7627	8.6	8.3	424	(0.155, 0.054)	62	-
80 wt% *S*-BNPCN-*o*-TBCP: PPF	4.2	7603	8.0	7.9	424	(0.155, 0.055)	62	-
50 wt% *S*-BNPCN-*p*-TBCP: PPF	3.0	10920	6.7	6.6	428	(0.153, 0.066)	65	–1.82
60 wt% *S*-BNPCN-*p*-TBCP: PPF	3.0	12390	6.7	6.7	428	(0.153, 0.066)	65	-
70 wt% *S*-BNPCN-*p*-TBCP: PPF	3.0	13700	6.6	6.6	428	(0.152, 0.066)	65	-
80 wt% *S*-BNPCN-*p*-TBCP: PPF	3.0	14180	6.6	6.6	428	(0.153, 0.065)	63	-

[a)] Abbreviations: EML = emitting layer; V_{on} = turn-on voltage at 1 cd m^{-2}; L_{max} = maximum luminance; η_{ext} = external quantum efficiency; λ_{EL} = EL peak; CIE = Commission Internationale de I'Eclairage coordinates; FWHM = full width at half maximum; g_{EL} = EL dissymmetry factor, which is only measured for the devices with 50 wt% doping concentration. Device configuration: ITO/HATCN (5 nm)/TAPC (50 nm)/TcTa (5 nm)/*m*CP (5 nm)/EML (20 nm)/PPF (5 nm)/TmPyPB (30 nm)/LiF (1 nm)/Al.

Taking the advantage of excellent Φ_{PL}s and good g_{PL} values in neat films, these near ultraviolet CPL materials are initially employed as chiral emitters for nondoped CP-OLEDs with the configuration of ITO/HATCN (5 nm)/TAPC (50 nm)/TcTa (5 nm)/*m*CP (5 nm)/EML (20 nm)/PPF (5 nm)/TmPyPB (30 nm)/LiF (1 nm)/Al, in which their neat films serve as emitting layer (EML), hexaazatriphenylenehexacabonitrile (HATCN), tolylaminophenyl)cyclohexane (TAPC) and PPF act as hole injection, hole-transporting and hole-blocking layers, respectively, tris(4-(carbazol-9-yl)phenyl)amine (TcTa), 1,3-di(carbazol-9-yl)benzene (*m*CP) and 1,3,5-tri(m-pyrid-3-yl-phenyl)benzene (TmPyPB) work as exciton-blocking, electron-blocking and electron-transporting layers, respectively. *S*-BNPCN-*o*-CP and *S*-BNPCN-*p*-CP radiate near ultraviolet lights with EL peaks at 406 nm ($CIE_{x,y}$ = 0.160, 0.040) and 414 nm ($CIE_{x,y}$ = 0.158, 0.048), narrow FWHMs of 52 and 47 nm, and maximum luminance (L_{max})

of 4743 and 11570 cd m^{-2}, respectively (Fig. 4 and Table 2). Owing to the enhanced ICT effect, *S*-BNPCN-*o*-TBCP and *S*-BNPCN-*p*-TBCP show red-shifted EL peaks at 422 nm ($CIE_{x,y}$ = 0.156, 0.056) and 428 nm ($CIE_{x,y}$ = 0.154, 0.063), and increased FWHMs of 60 and 61 nm, respectively. The nondoped devices of *S*-BNPCN-*o*-CP and *S*-BNPCN-*p*-CP provide high $\eta_{ext,max}$s of 6.7% and 7.8%, respectively, and enjoy high efficiency stability with neglectable efficiency roll-offs of 1.5% and 0.0% at 1000 cd m^{-2} luminance. The devices of *S*-BNPCN-*o*-TBCP and *S*-BNPCN-*p*-TBCP also exhibit high $\eta_{ext,max}$s of 6.1% and 6.4% and tiny efficiency roll-offs of 3.2% and 0.0%, respectively, at 1000 cd m^{-2} luminance. The high and stable EL efficiencies should be attributed to not only the high solid-state Φ_{PL}s but also fast hRISC process that successfully improves triplet exciton utilization and alleviates triplet-triplet annihilation. Besides, all the *R*-enantiomers show similar EL performances to these *S*-enantiomers (Supplementary Table 7), and the nondoped device of *R*-BNPCN-*p*-CP achieves an impressive $\eta_{ext,max}$ as high as 8.0%

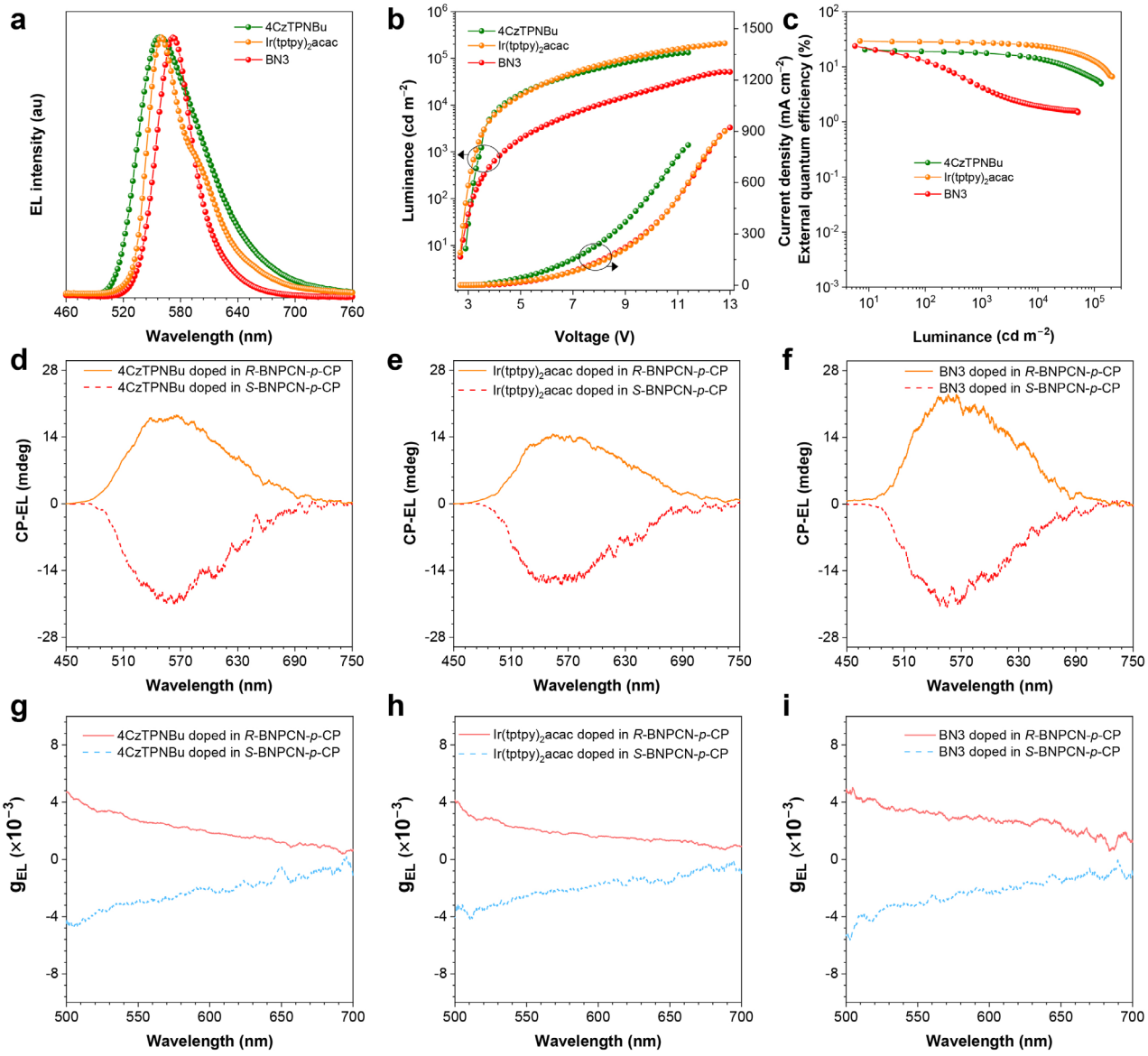

Fig. 5 | CP-EL performances of sensitized CP-OLEDs using *S*/*R*-BNPCN-*p*-CP as hosts. a, EL spectra of 4CzTPNBu (3 wt%), Ir(tptpy)2acac (3 wt%), BN3 (3 wt%) doped in *S*-BNPCN-*p*-CP at 5 V. **b**, Plots of luminance–voltage–current density and **c**, external quantum efficiency–luminance of doped OLEDs of 4CzTPNBu (3 wt%), Ir(tptpy)2acac (3 wt%), BN3 (3 wt%) doped in *S*-BNPCN-*p*-CP. CP-EL spectra of doped OLEDs of **d**, 4CzTPNBu (3 wt%), **e**, Ir(tptpy)2acac (3 wt%) and **f**, BN3 (3 wt%) doped in *S*/*R*-BNPCN-*p*-CP. Plots of g_{EL} versus EL wavelength of doped OLEDs of **g**, 4CzTPNBu (3 wt%), **h**, Ir(tptpy)2acac (3 wt%) and **i**, BN3 (3 wt%) doped in *S*/*R*-BNPCN-*p*-CP.

at 414 nm ($CIE_{x,y}$ = 0.157, 0.043; FWHM = 55 nm), without efficiency roll-off at 1000 cd m^{-2} luminance. Owing to their CP-PL nature, all the *S*/*R*-enantiomers exhibit good CP-EL signals (Fig. 4f and 4g), and their nondoped devices display mirror-image CP-EL spectra with high absolute EL dissymmetry factor ($|g_{EL}|$) values of up to 3.59 × 10^{-3} (Fig. 4e). To the best of our knowledge, these are the first examples for high-performance near ultraviolet nondoped CP-OLEDs reported so far.

To further explore the EL performance of these near ultraviolet CPL materials, their doped OLEDs are fabricated and investigated. The device configuration is the same as that of the nondoped device, except using their doped films as EMLs. Taking *S*-BNPCN-*o*-CP as an example, the host is optimized between *m*CP and PPF at a doping concentration of 50 wt% *S*-BNPCN-*o*-CP in low-polar *m*CP host shows a bluer EL peak at 396 nm and a narrower FWHM of 46 nm relative to those in high-polar PPF host (EL peak = 404 nm; FWHM = 54 nm), but the $\eta_{ext,max}$ is increased from 7.1% in *m*CP host to 8.7% in PPF host (Supplementary Table 8). Then, by increasing doping concentration from 10 to 80 wt% in PPF host, the doped devices of *S*-BNPCN-*o*-CP show red-shifted EL peaks from 388 nm ($CIE_{x,y}$ = 0.161, 0.032) to 406 nm ($CIE_{x,y}$ = 0.158, 0.037) (Table 2, Supplementary Fig. S17 and Table 8). And the $\eta_{ext,max}$s change little, with a peak value of 9.0% at 60 wt% doping concentration. Similar trends are observed for other *S*-enantiomers. The $\eta_{ext,max}$s and EL peaks of *S*-BNPCN-*p*-CP, *S*-BNPCN-*o*-TBCP and *S*-BNPCN-*p*-TBCP are 7.2% and 414 nm ($CIE_{x,y}$ = 0.157, 0.044), 9.1% and 420 nm ($CIE_{x,y}$ = 0.155, 0.052), and 6.7% and 428 nm ($CIE_{x,y}$ = 0.153, 0.066), respectively. These doped devices also hold great efficiency stability, with very small efficiency roll-offs 0–10.9% at 1000 cd m^{-2} luminance. Moreover, they exhibit good CP-EL signals as well, with $|g_{EL}|$ values of up to 2.02 × 10^{-3} (Supplementary Fig. S17). The *R*-enantiomers show similar EL results to the *S*-enantiomers (Supplementary Table 9). In general, the $\eta_{ext,max}$s are increased while the $|g_{EL}|$ values become smaller in doped devices relative to nondoped devices, probably due to the irregular arrangement of molecules in blended system. These near ultraviolet CP-OLEDs actually have realized the state-of-the-art EL performances with apparent CP-EL signals in similar color regions to date.

Table 3 | EL performances of OLEDs using *S*-BNPCN-*p*-CP or *S*-BNPCN-*o*-CP as host or sensitizer. [a)]

EML	V_{on} (V)	λ_{EL} (nm)	L_{max} (cd m^{-2})	$\eta_{C,max}$ (cd A^{-1})	$\eta_{P,max}$ (lm W^{-1})	$\eta_{ext,max}$ (%)	FWHM (nm)	g_{EL} (10^{-3})
3 wt% Ir(tptpy)$_2$acac: *S*-BNPCN-*p*-CP	2.7	560	209400	103.3	120.1	29.3	60	–2.32
3 wt% Ir(tptpy)$_2$acac: *R*-BNPCN-*p*-CP	2.6	560	176700	98.2	118.6	28.0	60	2.00
3 wt% 4CzTPNBu: *S*-BNPCN-*p*-CP	2.9	558	132500	66.9	72.4	20.4	80	–2.87
3 wt% 4CzTPNBu: *R*-BNPCN-*p*-CP	2.9	558	130300	57.6	62.4	17.4	80	2.58
3 wt% BN3: *S*-BNPCN-*p*-CP	2.7	572	51410	89.6	104.1	23.8	44	–2.70
3 wt% BN3: *R*-BNPCN-*p*-CP	2.7	568	64450	85.7	99.7	22.4	44	2.72
3 wt% BN3: 20 wt% *S*-BNPCN-*o*-CP: PPF	3.2	566	20710	100.5	98.6	30.8	45	–1.17
3 wt% BN3: 20 wt% *R*-BNPCN-*o*-CP: PPF	3.2	566	15490	96.2	94.4	29.5	45	1.31

[a)] Abbreviations: V_{on} = turn-on voltage at 1 cd m^{-2}; $\eta_{C,max}$ = maximum current efficiency; $\eta_{P,max}$ = maximum power efficiency; $\eta_{ext,max}$ = maximum external quantum efficiency; L_{max} = maximum luminance; CIE = Commission International de l'Eclairage coordinates; λ_{EL} = EL peak. Device configuration: ITO/HATCN (5 nm)/TAPC (50 nm)/TcTa (5 nm)/*m*CP (5 nm)/EML (20 nm)/PPF (5 nm)/TmPyPB (30 nm)/LiF (1 nm)/Al. EML: light-emitting layer.

As discussed above, the achiral luminescent materials can acquire CP-PL signals via energy transfer from these near ultraviolet CPL materials. Encouraged by the impressive EL performance, it is envisioned that efficient CP-EL can be achieved for achiral luminescent materials by using these near ultraviolet CPL materials as hosts or sensitizers in OLEDs. As a proof concept, *S*-BNPCN-*p*-CP is adopted as the host and the typical TADF emitter (4CzTPNBu), MR-TADF emitter (BN3) and phosphorescence emitter (Ir(tptpy)$_2$acac) are selected as the guests for EL investigation in device of ITO/HATCN (5 nm)/TAPC (50 nm)/TcTa (5 nm)/*m*CP (5 nm)/EML (20 nm)/PPF (5 nm)/TmPyPB (30 nm)/LiF (1 nm)/Al. The doped films of Ir(tptpy)$_2$acac, 4CzTPNBu and BN3 in *S*-BNPCN-*p*-CP host at a concentration of 3 wt% work as EMLs. As shown in Fig. 5a, the devices of Ir(tptpy)$_2$acac, 4CzTPNBu and BN3 can

be turned on at 2.7–2.9 V and radiate yellow-orange lights with EL peaks at 560, 558 and 572 nm and FWHMs of 60, 80 and 44 nm, respectively (Table 3), which are in good agreement with their PL properties. The device of Ir(tptpy)$_2$acac attains remarkable L_{max}, maximum current efficiency ($\eta_{c,max}$), maximum power efficiency ($\eta_{P,max}$) and $\eta_{ext,max}$ of 209400 cd m^{-2}, 103.3 cd A^{-1}, 120.1 lm W^{-1} and 29.3%, respectively. The devices of 4CzTPNBu and BN3 also furnish excellent EL performances with L_{max}s of 132500 and 51410 cd m^{-2}, and $\eta_{ext,max}$s of 20.4% and 23.8%, respectively. The devices of Ir(tptpy)$_2$acac and 4CzTPNBu possess small efficiency roll-offs of 7.1% and 13.7%, respectively, at 1000 cd m^{-2} luminance (Fig. 5 and Supplementary Table 10). Moreover, the devices of Ir(tptpy)$_2$acac, 4CzTPNBu and BN3 display clear CP-EL signals with g_{EL} values of -2.32×10^{-3}, -2.87×10^{-3} and -2.70×10^{-3},

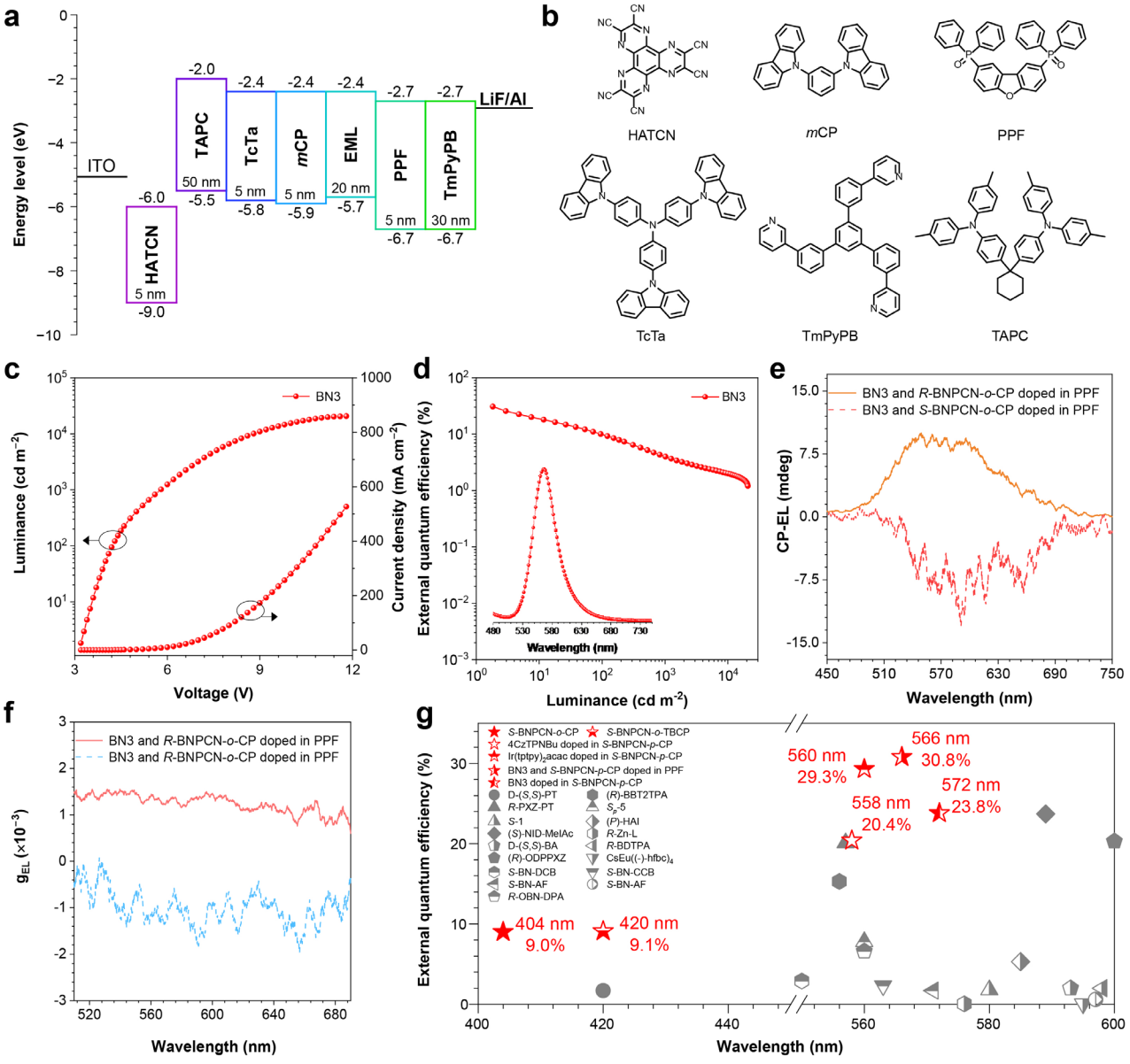

Fig. 6 | CP-EL performances of sensitized CP-OLEDs using *S*/*R*-BNPCN-*o*-CP as sensitizers. a, Schematic diagram of device energy levels and **b**, chemical structures of functional layers. Plots of **c**, luminance-voltage-current density and **d**, external quantum efficiency-luminance of doped OLEDs of BN3 (3 wt%): *S*-BNPCN-*p*-CP (20 wt%): PPF, inset plot is electroluminescence spectra of doped OLEDs of BN3 (3 wt%): *S*-BNPCN-*p*-CP (20 wt%): PPF at 5 V. **e**, CP-EL spectra and **f**, plots of g_{EL} versus EL wavelength of doped OLEDs of BN3 (3 wt%): *S*/*R*-BNPCN-*p*-CP (20 wt%): PPF. **g**, Reported maximum external quantum efficiencies of CP-OLEDs with EL peaks in the range of 400–450 nm and 550–600 nm.

respectively (Fig. 5). *R*-BNPCN-*p*-CP also serves well as host for these achiral luminescent materials, providing comparable CP-EL performances (Table 3).

In addition, these near ultraviolet CPL materials can function as sensitizers for achiral luminescent materials to obtain CP-EL as well. For instance, the doped devices with the configuration of ITO/HATCN (5 nm)/TAPC (50 nm)/TcTa (5 nm)/*m*CP (5 nm)/EML (20 nm)/PPF (5 nm)/TmPyPB (30 nm)/LiF (1 nm)/Al are fabricated (Fig. 6a and 6b). The EML is composed of the doped film of BN3 (3 wt%) and *S*-BNPCN-*o*-CP (20 wt%) in PPF host, where *S*-BNPCN-*o*-CP is used to sensitize BN3. As shown in Fig. 6c, the device of BN3 with *S*-BNPCN-*p*-CP as sensitizer shows an EL peak at 566 nm with narrow FWHM of 45 nm, similar to the PL property of BN3. Superb L_{max} of 20710 cd m^{-2} and $\eta_{ext,max}$ of 30.8% are attained, and distinct CP-EL signal with a g_{EL} of -1.17×10^{-3} is recorded. *R*-BNPCN-*p*-CP can offer comparable performance as the sensitizer for BN3 (Table 3). These devices are the most efficient sensitized CP-OLEDs in similar color regions in the literature (Fig. 6g and Supplementary Table 11).

Discussion

In summary, as a proof of concept, the one-to-many strategy for realizing CP-EL is proposed based on energy and chirality transfer from short-wavelength CPL materials to long-wavelength achiral luminescent materials that are rarely used to directly produce CP-EL in previous researches. Firstly, a series of efficient near ultraviolet CPL materials with high Φ_{PL}s and high exciton utilization based on hRISC process are explored by introducing chiral *S*/*R*-BN groups to the conjugated carbazole-phenyl-benzonitrile skeleton. The *S*/*R*-BN groups attached on benzonitrile acceptor can not only endow the molecule with CPL property but also weaken ICT effect to ensure short-wavelength emission. They can serve as light-emitting materials to fabricate highly efficient nondoped and doped near ultraviolet CP-OLEDs, providing large $|g_{EL}|$ values of up to 3.59×10^{-3} and outstanding $\eta_{ext,max}$s of 9.0% at 404 nm (CIE = 0.166, 0.066; FWHM = 54 nm) based on *S*-BNPCN-*o*-CP and 9.1% at 420 nm (CIE = 0.155, 0.052; FWHM = 62 nm) based on *S*-BNPCN-*o*-TBCP, with very small efficiency roll-offs, demonstrating they are the most efficient near ultraviolet CP-EL materials ever reported. Secondly, no matter in solutions or in neat and doped films, the developed near ultraviolet CPL materials can successfully sensitize different kinds of achiral fluorescence, phosphorescence, TADF and MR-TADF materials to generate blue to red CP-PL signals. Thirdly, yellow-orange CP-OLEDs are successfully achieved by adopting near ultraviolet CPL materials (*S*/*R*-BNPCN-*p*-CP) as hosts for achiral luminescent materials, including phosphorescence emitter (Ir(tptpy)$_2$acac), typical TADF emitter (4CzTPNBu) and MR-TADF emitter (BN3), furnishing good $|g_{EL}|$ values of up to 2.87×10^{-3} and excellent $\eta_{ext,max}$s of 29.3%, 20.4% and 23.8%, respectively. Finally, high-performance sensitized CP-OLEDs are fabricated by using *S*/*R*-BNPCN-*o*-CP as sensitizer for BN3 in PPF host, which provide good $|g_{EL}|$ value of 1.31×10^{-3} and outstanding $\eta_{ext,max}$ reaching 30.8% at 566 nm (FWHM = 45 nm). In view of the overlap of absorption spectra of achiral luminescent materials and the PL spectra of the near ultraviolet CPL materials, the FRET process may be accountable for the appearance of CP-PL and CP-EL signals of achiral luminescent materials. To the best of our knowledge, these CP-OLEDs with the near ultraviolet CPL materials as emitters, hosts or sensitizers are the best CP-OLEDs with apparent CP-EL signals in similar color regions reported so far. These results eloquently demonstrate the proposed one-to-many strategy for CP-EL is feasible and effective, and the robust short-wavelength CPL materials play a key role, by which different kinds of achiral luminescent material can be induced to exhibit CP-PL and CP-EL signals. This strategy could be a simple and universal approach for constructing muti-color high-performance CP-OLEDs with diverse well-developed, commercially available achiral EL materials, avoiding complicated synthetic works to create new CP-EL materials.

Data availability

The data that support the findings of this study are available from the corresponding authors on request. All data generated or analyzed during this study are included in this published article and its Supplementary Information.

References

1 Brandt, J. R., Salerno, F. & Fuchter, M. J. The added value of small-molecule chirality in technological applications. *Nat. Rev. Chem.* **1**, 0045 (2017).

2 Frédéric, L., Desmarchelier, A., Favereau, L. & Pieters, G. Designs and applications of circularly polarized thermally activated delayed fluorescence molecules. *Adv. Funct. Mater.* **31**, 2010281 (2021).

3 Kumar, J., Nakashima, T. & Kawai, T. Circularly polarized luminescence in chiral molecules and supramolecular assemblies. *J. Phys. Chem. Lett.* **6**, 3445-3452 (2015).

4 Stachelek, P., MacKenzie, L., Parker, D. & Pal, R. Circularly polarised luminescence laser scanning confocal microscopy to study live cell chiral molecular interactions. *Nat. Commun.* **13**, 553 (2022).

5 Parker, D., Fradgley, J. D. & Wong, K. L. The design of responsive luminescent lanthanide probes and sensors. *Chem. Soc. Rev.* **50**, 8193-8213 (2021).

6 Zhang, D. W., Li, M. & Chen, C. F. Recent advances in circularly polarized electroluminescence based on organic light-emitting diodes. *Chem. Soc. Rev.* **49**, 1331-1343 (2020).

7 Zinna, F. *et al.* Emergent nonreciprocal circularly polarized emission from an organic thin film. *Adv. Mater.* **32**, e2002575 (2020).

8 Yang, S. Y. *et al.* Circularly polarized thermally activated delayed fluorescence emitters in through-space charge transfer on asymmetric spiro skeletons. *J. Am. Chem. Soc.* **142**, 17756-17765 (2020).

9 Nishizawa, N., Nishibayashi, K. & Munekata, H. Pure circular polarization electroluminescence at room temperature with spin-polarized light-emitting diodes. *Proc. Natl. Acad. Sci. USA* **114**, 1783-1788 (2017).

10 Deng, Y. *et al.* Circularly polarized luminescence from organic micro-/nano-structures. *Light. Sci. Appl.* **10**, 76 (2021).

11 Dhbaibi, K. *et al.* Achieving high circularly polarized luminescence with push-pull helicenic systems: From rationalized design to top-emission cp-oled applications. *Chem. Sci.* **12**, 5522-5533 (2021).

12 Luo, X. F. *et al.* Multicolor circularly polarized photoluminescence and electroluminescence with 1,2-diaminecyclohexane enantiomers. *ACS Appl. Mater. Interfaces* **12**, 23172-23180 (2020).

13 Jiang, Z. *et al.* Rational design of axially chiral platinabinaphthalenes with aggregation-induced emission for red circularly polarized phosphorescent organic light-emitting diodes. *ACS Appl. Mater. Interfaces* **12**, 9520-9527 (2020).

14 Frédéric, L. *et al.* Maximizing chiral perturbation on thermally activated delayed fluorescence emitters and elaboration of the first top-emission circularly polarized oled. *Adv. Funct. Mater.* **30**, 2004838 (2020).

15 Lee, D. M., Song, J. W., Lee, Y. J., Yu, C. J. & Kim, J. H. Control of circularly polarized electroluminescence in induced twist structure of conjugate polymer. *Adv. Mater.* **29**, 1700907 (2017).

16 Zinna, F. *et al.* Design of lanthanide-based oleds with remarkable circularly polarized electroluminescence. *Adv. Funct. Mater.* **27**, 1603719 (2017).

17 Wan, L. *et al.* Highly efficient inverted circularly polarized organic light-emitting diodes. *ACS Appl. Mater. Interfaces* **12**, 39471-39478 (2020).

18 Qian, G. *et al.* Chiral platinum-based metallomesogens with highly efficient circularly polarized electroluminescence in solution-processed organic light-emitting diodes. *Adv. Optical Mater.* **8**, 2000775 (2020).

19 Song, F. *et al.* Highly efficient circularly polarized electroluminescence from aggregation-induced emission luminogens with amplified chirality and delayed fluorescence. *Adv. Funct. Mater.* **28**, 1800051 (2018).

20 Geng, Z., Zhang, Y., Zhang, Y., Quan, Y. & Cheng, Y. Amplified circularly polarized electroluminescence behavior triggered by helical nanofibers from chiral co-assembly polymers. *Angew. Chem. Int. Ed.* **61**, e202202718 (2022).

21 Tan, Y. B. *et al.* Visible circularly polarized luminescence of octanuclear circular Eu(iii) helicate. *J. Am. Chem.*

Soc. **142**, 17653-17661 (2020).

22 Jimenez, J. *et al.* Binolated aminostyryl bodipys: A workable organic molecular platform for NIR circularly polarized luminescence. *Chem. Commun.* **57**, 5750-5753 (2021).

23 Wu, Z. G. *et al.* Chiral octahydro-binaphthol compound-based thermally activated delayed fluorescence materials for circularly polarized electroluminescence with superior eqe of 32.6% and extremely low efficiency roll-off. *Adv. Mater.* **31**, e1900524 (2019).

24 Li, M., Wang, Y. F., Zhang, D., Duan, L. & Chen, C. F. Axially chiral TADF-active enantiomers designed for efficient blue circularly polarized electroluminescence. *Angew. Chem. Int. Ed.* **59**, 3500-3504 (2020).

25 Yan, Z. P. *et al.* Chiral thermally activated delayed fluorescence materials based on *R*/*S*-N^2, $N^{2\prime}$-diphenyl-[1,1′-binaphthalene]-2,2′-diamine donor with narrow emission spectra for highly efficient circularly polarized electroluminescence. *Adv. Funct. Mater.* **31**, 2103875 (2021).

26 Wang, Y. *et al.* Circularly polarized electroluminescence of thermally activated delayed fluorescence-active chiral binaphthyl-based luminogens. *ACS Appl. Mater. Interfaces* **11**, 26165-26173 (2019).

27 Liao, C., Zhang, Y., Ye, S. H. & Zheng, W. H. Planar chiral [2.2]paracyclophane-based thermally activated delayed fluorescent materials for circularly polarized electroluminescence. *ACS Appl. Mater. Interfaces* **13**, 25186-25192 (2021).

28 Takaishi, K., Murakami, S., Yoshinami, F. & Ema, T. Binaphthyl-bridged pyrenophanes: Intense circularly polarized luminescence based on a D_2 symmetry strategy. *Angew. Chem. Int. Ed.* **61**, e202204609 (2022).

29 Krishnadas, K. R. *et al.* Chiral functionalization of an atomically precise noble metal cluster: Insights into the origin of chirality and photoluminescence. *ACS Nano* **14**, 9687-9700 (2020).

30 Wade, J. *et al.* 500-fold amplification of small molecule circularly polarised luminescence through circularly polarised fret. *Angew. Chem. Int. Ed.* **60**, 222-227 (2021).

31 Yang, D., Duan, P., Zhang, L. & Liu, M. Chirality and energy transfer amplified circularly polarized luminescence in composite nanohelix. *Nat. Commun.* **8**, 15727 (2017).

32 Zhao, T., Han, J., Duan, P. & Liu, M. New perspectives to trigger and modulate circularly polarized luminescence of complex and aggregated systems: Energy transfer, photon upconversion, charge transfer, and organic radical. *Acc. Chem. Res.* **53**, 1279-1292 (2020).

33 Bene, L., Bagdany, M. & Damjanovich, L. Checkpoint for helicity conservation in fluorescence at the nanoscale: Energy and helicity transfer (hfret) from a rotating donor dipole. *Biophys. Chem.* **239**, 38-53 (2018).

34 Sharma, N. *et al.* Turn on of sky-blue thermally activated delayed fluorescence and circularly polarized luminescence (CPL) via increased torsion by a bulky carbazolophane donor. *Chem. Sci.* **10**, 6689-6696 (2019).

35 Yang, Z. *et al.* Recent advances in organic thermally activated delayed fluorescence materials. *Chem. Soc. Rev.* **46**, 915-1016 (2017).

36 Xu, Z., Tang, B. Z., Wang, Y. & Ma, D. Recent advances in high performance blue organic light-emitting diodes based on fluorescence emitters. *J. Mater. Chem. C* **8**, 2614-2642 (2020).

37 Khan, A. *et al.* Intramolecular-locked high efficiency ultrapure violet-blue (CIE-y <0.046) thermally activated delayed fluorescence emitters exhibiting amplified spontaneous emission. *Adv. Funct. Mater.* **31**, 2009488 (2021).

38 Yan, Z. P. *et al.* A chiral dual-core organoboron structure realizes dual-channel enhanced ultrapure blue emission and highly efficient circularly polarized electroluminescence. *Adv. Mater.* e2204253 (2022).

39 Yang, Y. *et al.* Chiral multi-resonance TADF emitters exhibiting narrowband circularly polarized electroluminescence with an eqe of 37.2%. *Angew. Chem. Int. Ed.* **61**, e202202227 (2022).

40 Zhou, L. *et al.* Tetracoordinate boron-based multifunctional chiral thermally activated delayed fluorescence emitters. *Angew. Chem. Int. Ed.* **61**, e202203844 (2022).

41 Wu, X. *et al.* Fabrication of circularly polarized MR-TADF emitters with asymmetrical peripheral-lock enhancing helical b/n-doped nanographenes. *Adv. Mater.* **34**, e2105080 (2022).
42 Lu, T. & Chen, F. Multiwfn: A multifunctional wavefunction analyzer. *J. Comput. Chem.* **33**, 580-592 (2012).
43 Zhang, T. *et al.* Using the isotope effect to probe an aggregation induced emission mechanism: Theoretical prediction and experimental validation. *Chem. Sci.* **7**, 5573-5580 (2016).
44 Chen, J. *et al.* Robust luminescent molecules with high-level reverse intersystem crossing for efficient near ultraviolet organic light-emitting diodes. *Angew. Chem. Int. Ed.* **61**, e202116810 (2022).
45 Guo, X. *et al.* Unraveling the important role of high-lying triplet-lowest excited singlet transitions in achieving highly efficient deep-blue AIE-based oleds. *Adv. Mater.* **33**, e2006953 (2021).
46 Xu, Y. *et al.* Highly efficient blue fluorescent oleds based on upper level triplet-singlet intersystem crossing. *Adv. Mater.* **31**, e1807388 (2019).
47 Zhang, S. *et al.* Achieving a significantly increased efficiency in nondoped pure blue fluorescent oled: a quasi-equivalent hybridized excited state. *Adv. Funct. Mater.* **25**, 1755-1762 (2015).
48 Kong, F. C. *et al.* Highly efficient sensitized chiral hybridized local and charge-transfer emitter circularly polarized electroluminescence. *Adv. Funct. Mater.* **32**, 2201512 (2022).
49 Steinberg, I. Z. & Ehrenberg, B. A theoretical evaluation of the effect of photoselection on the measurement of the circular polarization of luminescence. *J. Chem. Phys.* **61**, 3382 (1974).
50 Yao, K., Li, Y., Shen, Y., Quan, Y. & Cheng, Y. A photosensitive-type CPL response controlled by intermolecular dynamic FRET and chiral transfer in ternary chiral emissive nematic liquid crystals. *J. Mater. Chem. C* **9**, 12590-12595 (2021).
51 Han, D. *et al.* Sequentially amplified circularly polarized ultraviolet luminescence for enantioselective photopolymerization. *Nat. Commun.* **11**, 5659 (2020).
52 Hong, J. *et al.* Chiral polymer hosts for circularly polarized electroluminescence devices. *Chem. Sci.* **12**, 8668-8681 (2021).
53 Di Nuzzo, D. *et al.* High circular polarization of electroluminescence achieved via self-assembly of a light-emitting chiral conjugated polymer into multidomain cholesteric films. *ACS Nano* **11**, 12713-12722 (2017).
54 Sang, Y., Han, J., Zhao, T., Duan, P. & Liu, M. Circularly polarized luminescence in nanoassemblies: Generation, amplification, and application. *Adv. Mater.* **32**, 1900110 (2019).
55 Zhao, T., Han, J., Shi, Y., Zhou, J. & Duan, P. Multi-light-responsive upconversion-and-downshifting-based circularly polarized luminescent switches in chiral metal-organic frameworks. *Adv. Mater.* e2101797 (2021).
56 Yao, K. *et al.* Ultrastrong red circularly polarized luminescence promoted from chiral transfer and intermolecular forster resonance energy transfer in ternary chiral emissive nematic liquid crystals. *J. Phys. Chem. Lett.* **12**, 598-603 (2021).
57 Li, M., Wang, M. Y., Wang, Y. F., Feng, L. & Chen, C. F. High-efficiency circularly polarized electroluminescence from TADF-sensitized fluorescent enantiomers. *Angew. Chem. Int. Ed.* **60**, 20728-20733 (2021).
58 Yang, C., Chen, W., Zhu, X., Song, X. & Liu, M. Self-assembly and circularly polarized luminescence from achiral pyrene-adamantane conjugates by selective inclusion with cyclodextrins. *J. Phys. Chem. Lett.* **12**, 7491-7496 (2021).
59 Cheng, Q., Hao, A. & Xing, P. Eutectogels as matrices to manipulate supramolecular chirality and circularly polarized luminescence. *ACS Nano* **16**, 6825−6834 (2022).
60 Forbes, K. A., Bradshaw, D. S. & Andrews, D. L. Influence of chirality on fluorescence and resonance energy transfer. *J. Chem. Phys.* **151**, 034305 (2019).

Methods

General information

All the synthesis experiments were performed under nitrogen atmosphere. All the chemicals and reagents were purchased from commercial sources and used as received without further purification. The final products were subjected to vacuum sublimation to further improve purity before PL and EL properties investigations. NMR spectra were measured on a Bruker Avance-500 spectrometer in the solvents indicated. High-resolution mass spectra (HRMS) were recorded on a GCT premier CAB048 mass spectrometer operating in MALDI-TOF mode. All the crystal samples were obtained in dichloromethane/hexane at room temperature. The single crystal X-ray diffraction intensity data were collected at 173 K on a Bruker–Nonices Smart Apex CCD diffractometer with graphite monochromated MoKα radiation. Processing of the intensity data was carried out using the SAINT and SADABS routines, and the structure and refinement were conducted using the SHELTL suite of X-ray programs (version 6.10). Cyclic voltammogram was measured in a solution of tetra-*n*-butylammonium hexafluorophosphate (Bu_4NPF_6, 0.1 M) in dichloromethane and *N*,*N*-dimethylformamide containing the sample at a scan rate of 50 mV s^{-1}. Three-electrode system (Ag/Ag^+, platinum wire and glassy carbon electrode as reference, counter and work electrode respectively) was used in the cyclic voltammetry measurement to determine HOMO and LUMO energy levels (HOMO = –[E_{ox} + 4.8] eV, and LUMO = –[E_{re} + 4.8] eV). E_{ox} and E_{re} represent the onset oxidation and reduction potentials relative to ferrocene, respectively. The ground-state geometries were optimized using the density function theory (DFT) method with M06-2X functional at the basis set level of 6-31G (d,p). All the calculations were performed using Gaussian16 package.

Photophysical property measurement

UV-vis absorption spectra were measured on a Shimadzu UV-2600 spectrophotometer. PL spectra were recorded on a Horiba Fluoromax-4 spectrofluorometer. Fluorescence quantum yields were measured using a Hamamatsu absolute PL quantum yield spectrometer C11347 Quantaurus_QY. Transient PL decay spectra were measured under nitrogen atmosphere (solution) or vacuum (neat film), using Quantaurus-Tau fluorescence lifetime measurement system (C11367-03, Hamamatsu Photonics Co., Japan). Circular dichroism (CD) spectra were recorded with a Chirascan spectrometer (Applied Photophysics, England). Circularly polarized photoluminescence (CP-PL) and circularly polarized electroluminescence (CP-EL) spectra were recorded at 100 nm min^{-1} scan speed with a commercialized instrument JASCO CPL-300 at room temperature. The CP-PL and CP-EL spectra of each simple were further examined by rotation 90° and 180°, the profiles were almost the same with 0°.

OLED fabrication and characterization

Glass substrates pre-coated with a 90-nm-thin layer of indium tin oxide (ITO) with a sheet resistance of 20 Ω per square were thoroughly cleaned for 10 minutes in ultrasonic bath of acetone, isopropyl alcohol, detergent, deionized water, and isopropyl alcohol and then treated with O_2 plasma for 5 min in sequence. Organic layers were deposited onto the ITO-coated substrates by high-vacuum (< 5×10^{-4} Pa) thermal evaporation. Deposition rates were controlled by independent quartz crystal oscillators, which are 1~2 Å s^{-1} for organic materials, 0.2 Å s^{-1} for LiF, and 5 Å s^{-1} for Al, respectively. The emission area of the device is 3×3 mm^{-2} as shaped by the overlapping area of the anode and cathode. All the device characterization steps were carried out at room temperature under ambient laboratory conditions without encapsulation. The luminance–voltage–current density and external quantum efficiency were characterized with a dual-channel Keithley 2614B source meter and a PIN-25D silicon photodiode. The electroluminescence spectra were obtained via an Ocean Optics USB 2000+ spectrometer, along with a Keithley 2614B Source Meter.

Acknowledgements

This work was financially supported by the National Natural Science Foundation of China (21788102), the Natural Science Foundation of Guangdong Province (2022A1515010315, 2019B030301003, 2021A1515110826) and the

Science and Technology Program of Guangzhou, China (202201010439).

Author contributions

L.X. and H.L. contributed equally to this work. Z.Z. conceived the study. L.X. synthesized and characterized the materials, measured the photophysical property. H.L. fabricated and characterized the OLEDs. X.P. and P.S. performed theoretical simulation. L.X. and Z.Z. wrote and revised the manuscript. Z.Z. and B.Z.T. supervised the project. All authors discussed the results and commented on the manuscript. / All authors have given approval to the final version of the manuscript.

Competing interests

The authors declare no competing interests.

Additional information

Supplementary information is available for this paper.